




Preparation of hierarchical porous activated carbons for high performance supercapacitors from coal gasification fine slag

Shanxin Xiong^{1,2,*} , Nana Yang¹, Xiaoqin Wang¹, Ming Gong¹, Jia Chu¹, Runlan Zhang¹, Bohua Wu¹, Zhen Li¹, and Jianwei Xu³

¹ College of Chemistry and Chemical Engineering, Xi'an University of Science and Technology, Xi'an 710054, People's Republic of China

² Key Laboratory of Coal Resources Exploration and Comprehensive Utilization, Ministry of Land and Resources, Xi'an 710021, People's Republic of China

³ Institute of Materials Research and Engineering (IMRE), Agency for Science, Technology and Research (A*STAR), Singapore 138634, Singapore

Received: 11 March 2022

Accepted: 5 May 2022

Published online:
24 May 2022

© The Author(s), under exclusive licence to Springer Science+Business Media, LLC, part of Springer Nature 2022

ABSTRACT

Coal gasification is an important technology for clean conversion and utilization of coal. The coal gasification slag is the main solid waste of coal chemical industry, whose comprehensive utilization is an important factor for the whole coal chemical project to realize circular economy. In this work, coal gasification fine slag with high carbon content was used as the raw material to prepare hierarchical porous activated carbons (AC) after deep deashing. The optimal coal gasification fine slag activated carbon (GCFS-AC) has large BET surface area of 1151.8 m²/g and high total pore volume of 0.923 cm³/g. Owing to the hierarchical porous structures with large mesopore volume, CGFS-AC exhibits high charge storage capacity and energy density, as well as excellent cycling stability. The specific capacitance is 255.2 F/g at 1 A/g, which is significantly higher than that of commercial YP50 activated carbon. After 10,000 cycles, the specific capacitance is still 197.1 F/g, which is 94.4% of its initial capacitance. In addition, the CGFS-AC//CGFS-AC symmetric supercapacitor has a high energy density of 22.2 Wh/kg at power density of 399.8 W/kg.

1 Introduction

The coal gasification is the main and important process of coal chemical industry [1, 2]. The gasification residue or ash that consists of incompletely reacted

carbon and minerals in coal has become the largest solid waste in the coal chemical industry [3]. A large number of untreated gasification slag can pollute the water and atmosphere, and affect the sustainable development of coal chemical companies [4, 5].

Address correspondence to E-mail: xiongsx@xust.edu.cn

Therefore, the affective utilization of coal gasification slag (CGS) is imminent.

In order to achieve “zero emissions” for coal gasification technology, it is necessary to solve and develop the environmentally safe use of gasification slag [6]. The effective and comprehensive utilization of CGS not only reduces landfill requirements, but also improves economy benefit. The chemical and mineral composition of CGS are the basis of its comprehensive utilization. The CGS is mainly composed of unburned carbon, amorphous molten glass, and incompletely reacted mineral crystals. At present, the application of CGS at home and abroad is mainly concentrated in: construction materials [7, 8], water and soil remediation, residual carbon utilization [9], silicon-based material [10, 11], ceramic materials [12, 13], catalysts [14–16], and other high value-added materials [17]. However, CGS has high residual carbon content, which is not conducive to its application in construction materials.

Some researchers have reported that coal and coal-based materials can be used to prepare activated carbon [18–21]. Considering that the residual carbon of CGS has suffered carbonization process and possesses primary pore structure, CGS can be used as a suitable raw material for preparation of activated carbon [3, 5, 9, 22]. CGS can be divided into coarse slag (CS) and fine slag (FS). Among them, the CS is fetched from the lock hopper, while the FS exits with the syngas [2, 23]. Because of the different formation processes of CS and FS, the carbon content in them is also different [3]. The carbon content in the FS is significantly higher than that in the CS, and it has highly developed pore structure [2, 24]. The carbon component of coal gasification fine slag (CGFS) has completed the carbonization process in the coal gasification process and only needs direct activation for preparation of activated carbon [24, 25]. Up to now, only few researchers have studied the preparation of activated carbon from CGS. Xu et al. [26] used CGS as precursor to prepare highly porous activated carbons with BET surface area and total pore volume as high as 2481 m²/g and 1.711 cc/g by KOH activation, which was used to remove Pb²⁺ from aqueous solution. Miao et al. [27] fabricated FS-based ACs for CO₂ capture with a specific surface area of 1187 m²/g and a pore volume of 0.89 cm³/g through KOH activation. However, research on the application of CGFS-based activated carbon in supercapacitor electrode materials is few reported. The ash in the CGFS-based activated carbon

not only increases the resistance and voltage drop of the electrode material, but also reduces the power density of supercapacitor and generates leakage current, which will affect the cycling stability of the supercapacitor. Zhao et al. [28] prepared coal-based carbon activated nanofibers from coal of Dahuangshan by deashing with HNO₃ (63%) and H₂SO₄ (98%) (volume ratio 1:3) mixture and then treated with steam. The specific capacitance of obtained activated nanofibers is 230 F/g at 1 A/g. Dong et al. [29] prepared interconnected porous carbon nanosheet/nickel foam (PCNS/NF) composites using coal tar pitch as carbon precursor and KOH as activation reagent, then washed sequentially by 0.1 M NaOH and 0.05 M HCl, which exhibited high specific capacitance of 3000 mF/cm² at 0.6 mA/cm².

Considering all these in mind, a kind of AC with interconnected macropores and micro-mesopores structure was fabricated from industrial solid waste CGFS and used as supercapacitor electrode materials, which will offer a new path for utilization of CGFS with high additional value. In this paper, the effects of the GCFS/KOH mass ratio on structures and capacitance performances of GCFS-AC have been investigated. The activated carbon prepared under the optimal conditions was assembled into a symmetrical capacitor and its capacitance performance was studied. It is found that this capacitor has high specific capacitance, energy density, and excellent cycling stability. Therefore, a low-cost and environmentally friendly electrode material can be provided for high-energy-density supercapacitors.

2 Experimental

2.1 Materials

CGFS sample was taken from the Shenhua Shenmu Chemical Industry Co., China. Its proximate analysis, ultimate analysis, and loss on ignition are shown in Table 1. H₂SO₄, HCl, HF, HNO₃, KOH, and NaOH were purchased from local reagent suppliers and used without any further purification. Super-P conductive carbon black (Super-P) was purchased from Timcal Graphite Co., Switzerland. Polyvinylidene fluoride (Solef 5130-PVDF) was bought from Solvay Co., France. Graphite papers with 0.05 mm thickness were bought from Qindao Huatai Lubrication & Sealing Technology Co., China.

2.2 Deashing treatment of coal gasification fine slag

In order to reduce the negative influences of minerals on the electrode material, demineralization of CGFS was conducted with different methods. Firstly, the CGFS was crushed with a crusher, and milled with a planetary ball mill at 870 r for 4 h, and then a 200-standard sieve was used to remove the part with a particle size less than 75 μm . Then, the CGFS was stirred in different concentrations (10%, 20%, and 30%) of acid (HCl, HF, HNO_3 , or H_2SO_4), alkali (NaOH or KOH), mixed acid (HCl and other acids, including HF, HNO_3 , or H_2SO_4), or two-step acid (Firstly, CGFS was mixed and stirred in 30% HCl at room temperature for 4 h and washed to neutrality. Then, it was mixed and stirred in different concentrations (10%, 20%, and 30%) of HF, HNO_3 , or H_2SO_4 , respectively) at room temperature for 4 h, where the liquid–solid ratio was 20. The sample was filtered and washed with deionized water several times until pH value was equal to 7. Afterward, the deashing CGFS was achieved after dried overnight at 80 $^\circ\text{C}$ in vacuum oven.

2.3 Activation process of coal gasification fine slag

Activated carbons preparation was carried out by chemical activation using KOH. Firstly, the deashing CGFS and KOH were mixed fully with weight ratios of 1:2, 1:3, 1:4, 1:5, and 1:6, respectively, and transferred into a graphite boat. Subsequently, the mixtures were calcined at a constant heating rate of 10 $^\circ\text{C}/\text{min}$ to 800 $^\circ\text{C}$ and then maintained 90 min in a cylindrical horizontal furnace, under an 80 mL/min N_2 flow. The obtained coal gasification fine slag-based activated carbon (CGFS-AC) was soaked in 10% HCl aqueous solution to remove the remaining activation agent and impurities followed by washing with deionized water several times until the filtrate was neutral and then dried at 80 $^\circ\text{C}$ for 12 h.

Table 1 Proximate analysis, ultimate analysis, and loss on ignition of CGFS

Proximate analysis (%)				Ultimate analysis (%)			Loss on ignition (%)
M_{ad}	A_{ad}	V_{ad}	FC_{ad}	C_{d}	H_{d}	N_{d}	
5.50	66.35	6.47	21.68	36.61	0.609	0.767	35.5%

“ M_{ad} ” is “moisture on an air dry basis,” “ A_{ad} ” is “ash on an air dry basis,” “ V_{ad} ” is “volatiles on an air dry basis,” and “ FC_{ad} ” is “fixed carbon on an air dry basis”

2.4 Characterization

The morphologies of samples were observed on a Phenom/Pro scanning electron microscopy. N_2 adsorption–desorption isotherms were obtained after degassing at 200 $^\circ\text{C}$ for 12 h using Micromeritics ASAP2020 automatic physical adsorption apparatus to study the textural structures of the materials and they were used to get the specific surface area by Brunauer–Emmett–Teller (BET) method. XRD analysis was used to determine the structure and crystalline of the samples by an UltimaIV diffractometer with $\text{Cu K}\alpha$ (0.15406 nm) radiation. FTIR spectra was collected on a PerkinElmer GX spectrometer in a wavenumber range of 400–4000 cm^{-1} . Raman spectra was performed in a Renishaw InVia Raman spectrometer with 532 nm laser as the source.

Electrochemical performances of samples were investigated using a CHI660E electrochemical workstation at room temperature. Electrochemical behaviors of samples were demonstrated by cyclic voltammetry (CV), galvanostatic charge and discharge (GCD), and electrochemical impedance spectroscopy (EIS) tests in a 6 M KOH aqueous electrolyte, using a three-electrode system and a two-electrode symmetric system, respectively. Active electrodes were coated on graphite papers. Therein, active materials (GCFS-AC), Super-P particles, and PVDF were mixed in DMF at a mass ratio of 8:1:1. For three-electrode system, platinum plate, Hg/HgO electrode, and as-fabricated active electrodes were offered as counter electrodes, reference electrodes, and working electrodes, respectively. CV and GCD measurements were carried out in a potential window from -1 V to 0 V. For two-electrode system, a symmetric supercapacitor was assembled using the GCFS-AC (CGFS/KOH is 1:4) as positive electrode and negative electrode. CV and GCD tests were conducted in a potential window from 0 V to 1.6 V. EIS measurements were performed between 100 kHz and 0.01 Hz at an open circuit potential in three-electrode or two-electrode systems. In addition, the specific capacitance, energy density,

power density, and coulombic efficiency in the article were calculated by referring to the equations in the literature [30].

3 Results and discussion

3.1 Deashing study of CGFS

In order to elucidate the influences of different deashing methods on minerals, demineralization of CGFS is conducted with acid treatment, alkali treatment, mixed acid treatment, and two-step acid treatment employing the method of magnetic stirring at room temperature. The results of CGFS ash content are shown in Tables 2 and 3. From the results in Table 2, it can be found that the alkaline solution has little effect on the ash content of CGFS, while the effect of acid treatment is much better. In contrast, with same concentration, HCl treatment has the most obvious deashing effect, followed by HF, because HCl can remove carbonates, phosphates, and alkaline minerals in CGFS, and HF can remove most of the substances, except for pyrite. However, the lowest ash content of single acid base treatment is 10.11%, which does not meet the requirements of ash content of supercapacitive electrode material (ash content less than 0.5%), so further deashing treatment is needed.

As can be seen from Table 3 that the ash content of CGFS after deashing with mixed acid still does not meet the requirements. The lowest ash content can be also obtained by the mixed treatment of HCl and HF. The mixed acid treatment does not exhibit better effect of deashing than single acid. It may be caused by the diluted effect of mixed solution and competitive ion dissociation degree of two acids, which reduces the reaction activity. Therefore, it is necessary to seek more effective deashing methods.

Table 2 Ash content of CGFS with treatment of different concentration of acid or alkali

	10%	20%	30%
HCl	34.91%	28.23%	10.11%
HF	36.81%	29.42%	14.32%
H ₂ SO ₄	43.91%	40.82%	40.21%
HNO ₃	39.82%	38.61%	34.93%
NaOH	60.47%	52.06%	50.42%
KOH	62.19%	58.57%	54.06%

Compared with all the results in Table 3, it can be found that the ash content of the two-step acid treatment is smaller because the alkali minerals and carbonates in CGFS can be removed by HCl first, and then other substances can be further removed by HF. From the above experiments, it is found that the best deashing method is treating with 30% HCl and 30% HF in order. Thus, a lowest ash content of 0.45% can be obtained.

3.2 Effect of CGFS/KOH mass ratio on textural properties of CGFS-AC

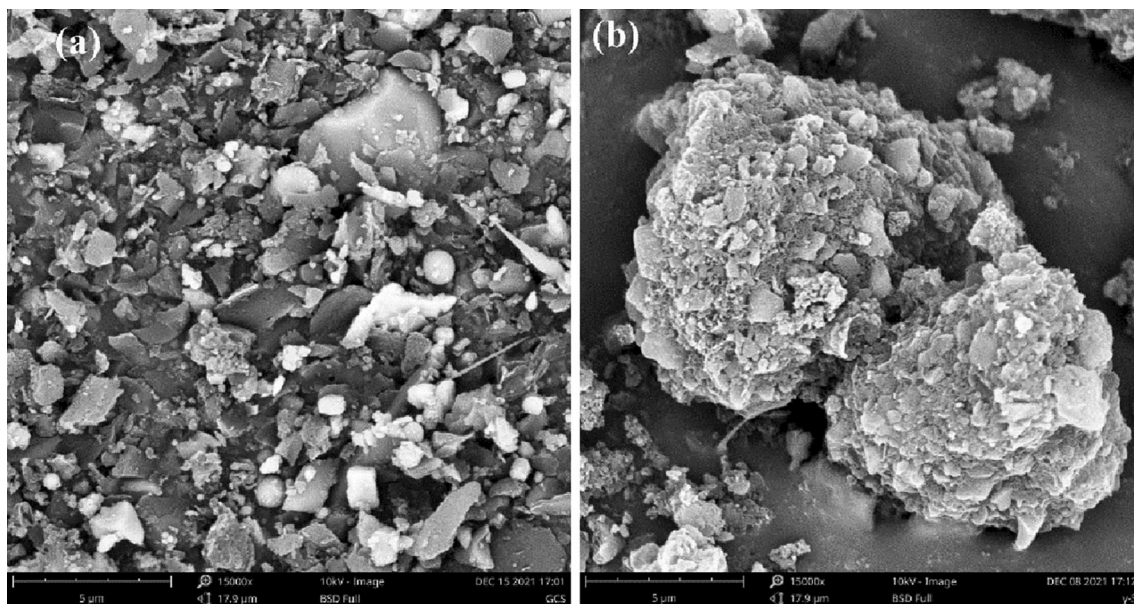
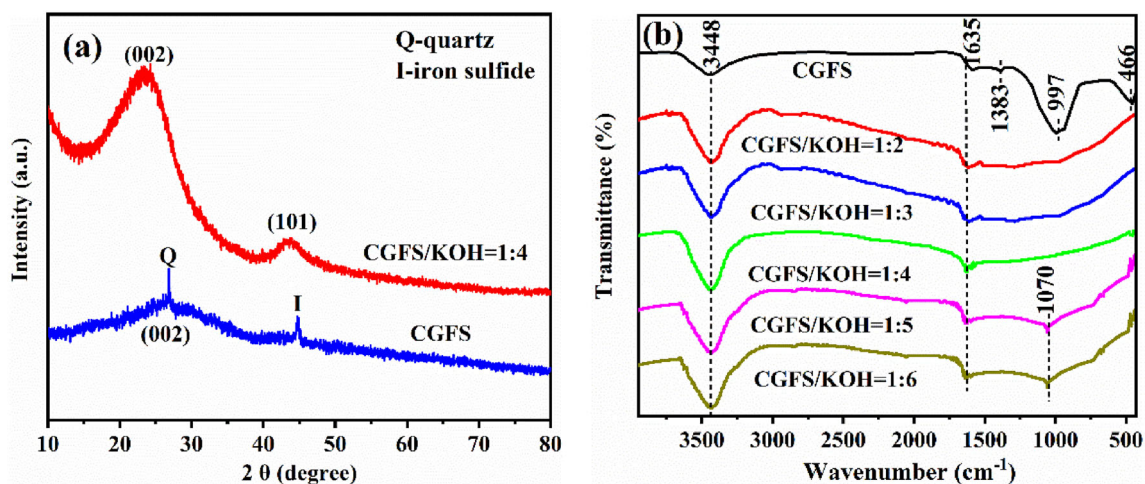
Figure 1 shows the surface morphologies of the CGFS (a) and CGFS-AC (1:4). CGFS sample is mainly composed of amorphous flocculent carbon and spherical or irregular inorganic particles, which are formed by melt of mineral at high temperature of gasification process. The morphology of CGFS after demineralization and activation is shown in Fig. 1b. Due to the removal of ash during the deashing process and the release of gas and volatile compounds during the activation process, most of melted inorganic particles are disappeared and porous carbon aggregation dominates the composition of CGFS-AC.

In order to understand the mineral composition and the structure of CGFS and CGFS-AC, XRD and FTIR analysis are presented in Fig. 2. XRD analysis shows that most of the substances in the CGFS exist in a glassy amorphous state, with only a small amount of quartz (SiO₂) and iron sulfide (FeS) crystals [24]. After demineralization and activation, the XRD pattern of the CGFS-AC sample shows broad peaks near 23° and 43°, corresponding to the (002) and (101) planes of graphite. It can be found that the (002) peak of the CGFS-AC sample shifted to a lower diffraction angle, indicating that the KOH activation of CGFS makes the graphene layer spacing larger (change from 0.335 nm to 0.384 nm) [31].

The surface functional groups of samples have effect on their electrochemical performance. The chemical structures of the CGFS and activated samples prepared under different conditions are further analyzed by the FTIR in Fig. 2b. A wide broad band is observed at 3448 cm⁻¹, which contributes to the typical O–H stretching vibrations of hydroxyl groups. The peak at 1635 cm⁻¹ confirms to the stretching vibration of C = C [32]. The peak at 1383 cm⁻¹ corresponds to the Si–O or Al–O [7, 19, 33]. The peak at 997 cm⁻¹ corresponds to the overlapping peak of the

Table 3 Ash content of CGFS after mixed acid treatment and two-step acid treatment with various acid concentrations

		10%	20%	30%
Mixed acid treatment	HCl + HF	16.57%	13.55%	10.19%
	HCl + H ₂ SO ₄	41.87%	40.12%	38.83%
	HCl + HNO ₃	35.21%	30.86%	28.12%
Two-step acid treatment	30%HCl → HF	0.85%	0.69%	0.45%
	30%HCl → H ₂ SO ₄	10.01%	9.84%	9.57%
	30%HCl → HNO ₃	9.85%	9.44%	8.87%

**Fig. 1** SEM of **a** CGFS and **b** CGFS-AC (1:4)**Fig. 2** **a** XRD patterns and **b** FTIR spectra of CGFS and CGFS-AC

stretching vibration of Si–O–Si and C–O–Si [26]. A peak at 466 cm^{-1} proves the existence of Si [26]. Although the activated samples in this work are prepared at different conditions, their FTIR spectra

are basically similar. As comparison with CGFS sample, some peaks of mineral are disappeared in the activated carbon. It is caused by the deashing of acid treatment. The over-dosed KOH will introduce

oxygen containing group into activated sample. The peak at 1070 cm^{-1} is related to the C–O stretching vibration in CGFS-AC (CGFS/KOH = 1:6 and 1:5) [34].

The microstructures of CGFS and CGFS-AC were analyzed by BET gas adsorption method. The N_2 adsorption–desorption isotherms and pore size distributions of CGFS and CGFS-AC are shown in Fig. 3. It can be seen from Fig. 3a that the adsorption capacity of the CGFS is very small, owing to that the porous residual carbon are embedded by melted mineral, which block the porous channel. When the mass ratio of KOH/CGFS increase from 2 to 3, the isotherms of the CGFS-AC samples have obvious hysteresis loops at P/P_0 range from 0.42 to 0.98, confirming that the material possesses silt-shaped micropores and small mesopores. When the mass ratio of KOH/CGFS reaches to 4, hysteretic plateau is disappeared from the middle section of the isotherm as shown in Fig. 3a and a peak appears in the pore size distribution figure at 20–40 nm as shown in Fig. 3b, indicating the existence of well-developed microporous and a large number of mesopores. When the mass ratio of KOH/CGFS in the range of 2–4, the main activation process is generation and expansion of pore structure. However, when the KOH/CGFS mass ratio continues to increase, the average pore size of the material increases, while S_{mic} , S_{BET} , and V_{mic}/V_t decrease, indicating that pore expansion rather than pore formation dominates the activation process in this stage. Table 4 presents the parameters of the pore structure of the CGFS-AC samples. As listed in Table 4, the specific surface area and pore volume first increase and then decrease

with the increase of KOH/CGFS ratio. This is due to the mechanism of pore formation is mainly the generation of H_2 , H_2O , CO , CO_2 , potassium oxide (K_2O), and potassium carbonate (K_2CO_3), in KOH activation of CGFS under high temperature pyrolysis. The cause of pore formation by KOH activated CGFS can be attributed to three aspects: (1) The process of H_2O and CO_2 generation that can promote pore development. (2) K_2O and K_2CO_3 are generated in the process of KOH corrosion of carbon skeleton, which is conducive to the formation of pore structure (3) K compounds (K_2O and K_2CO_3) are reduced into metal K by carbon, forming potassium vapor embedded into the carbon layer to form pores. When the mass ratio of KOH to CGFS is low, the K compounds (K_2O and K_2CO_3) and potassium vapors produced are not sufficient to completely corrode the carbon skeleton, only microporosity and a small amount of mesopores are produced. When the mass ratio of KOH to CGFS is higher, the reaction between KOH and CGFS is more complete and violent, and the redundant KOH can form potassium vapor and insert into the carbon lattice under high KOH load, resulting in over reaction and merging the existing pore structure, thus reducing the S_{BET} and V_{total} of the samples. Therefore, The CGFS-AC has the largest specific surface area ($1151.8\text{ m}^2/\text{g}$), highest pore volume ($0.923\text{ cm}^3/\text{g}$), and highest mesoporosity (78.5%), when the KOH/CGFS ratio is 4. Different from the traditional activated carbon materials with high specific surface area and high microporous volume, the CGFS-based activated carbon materials are hierarchical porous structures, which is beneficial to improve the specific surface area of the material and provides a mutually

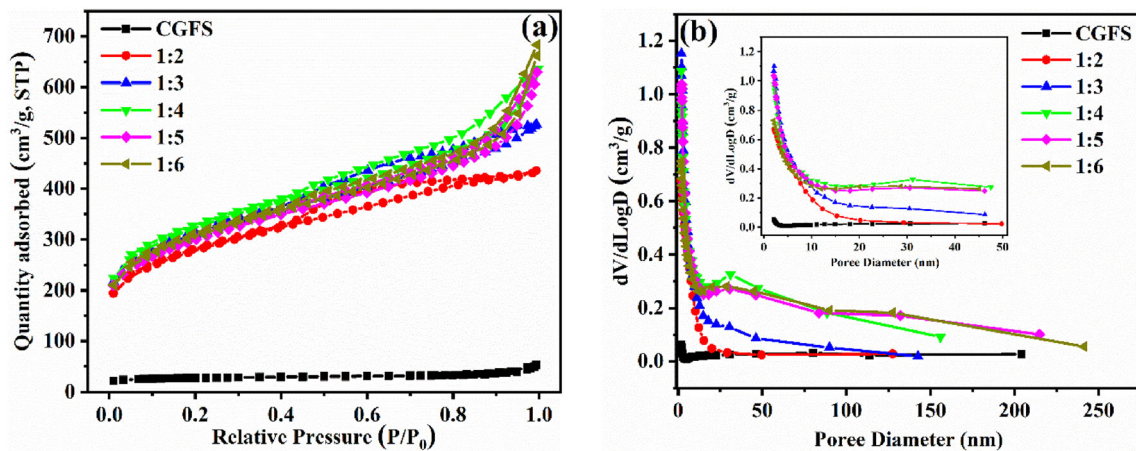


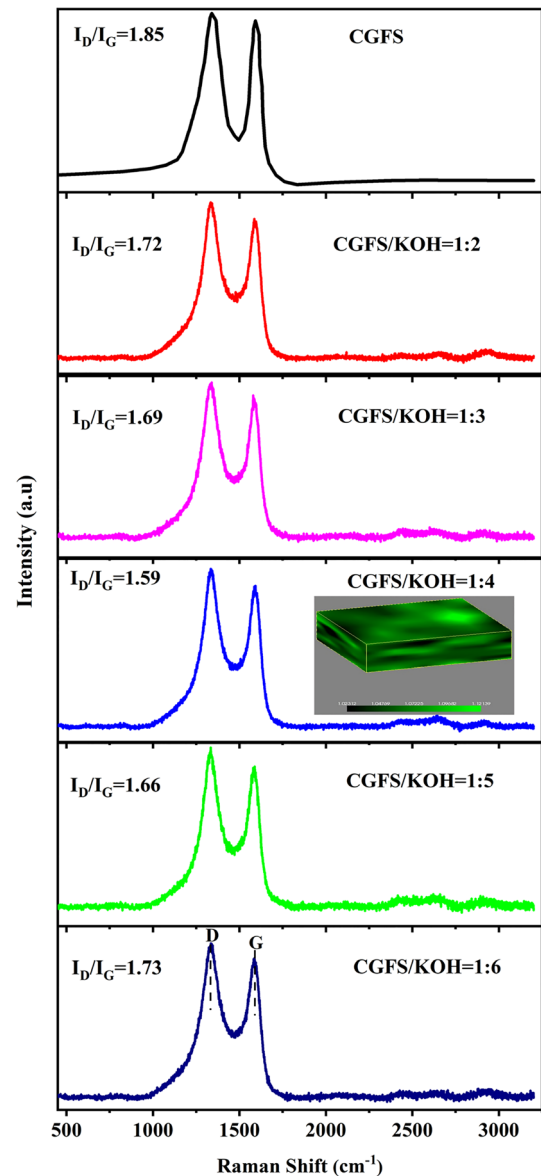
Fig. 3 a N_2 adsorption–desorption isotherms and b pore size distributions of CGFS and CGFS-AC, inset: an enlarged mesoporous section

Table 4 Specific surface area and pore structure of CGFS and CGFS-AC

Sample	S_{BET} (m^2/g)	S_{mic} (m^2/g)	V_{total} (cm^3/g)	V_{mic} (cm^3/g)	$V_{\text{mic}}/V_{\text{t}}$ (%)	Pore diameter (nm)
CGFS	93.29	60.71	0.076	0.028	36.84	3.29
CGFS/KOH = 1/2	991.93	353.56	0.762	0.150	19.68	2.64
CGFS/KOH = 1/3	1087.6	379.1	0.810	0.163	20.12	2.97
CGFS/KOH = 1/4	1151.8	437.8	0.923	0.187	20.26	3.04
CGFS/KOH = 1/5	1082.8	362.3	0.902	0.153	16.96	3.38
CGFS/KOH = 1/6	1043.5	346.9	0.896	0.151	16.85	3.54

connected channel for the transportation and storage of electrolyte ions.

The Raman spectra of the CGFS and CGFS-AC are shown in Fig. 4. The peaks at $\sim 1350 \text{ cm}^{-1}$ and $\sim 1590 \text{ cm}^{-1}$ correspond to the disorder induced peak (D peak) and graphitic peak (G peak), respectively. The D band is related to disordered graphite lattice, originating from the breathing mode of sixfold rings. The G band corresponds to the stretching vibration of the C = C sp^2 bond in graphene layer. The intensity ratio of two peaks ($I_{\text{D}}/I_{\text{G}}$) is commonly used to estimate the defect population or internal structure of carbon materials. The $I_{\text{D}}/I_{\text{G}}$ values of CGFS and CGFS-AC are 1.85, 1.72 (1:2), 1.69 (1:3), 1.59 (1:4), 1.66 (1:5), and 1.73 (1:6), respectively. The $I_{\text{D}}/I_{\text{G}}$ value of CGFS is the largest, which means that there are a lot of structural defects in the carbon skeleton of CGFS, formed by amorphous carbon with more sp^3 hybrid phases [35]. After the CGFS is pre-acidified and activated to remove the minerals, the graphite layer seems to be reorganized and the number of defects is reduced. With the increase of KOH/CGFS mass ratio, the $I_{\text{D}}/I_{\text{G}}$ value decreases first and then increases, indicating that the graphite carbon content in CGFS-AC increases first and then decreases, while the amorphous carbon content changes on the contrary. It is due to that when the of KOH/CGFS in the range of 2 to 4, the function of KOH is formation of pore network and pore development [24]. However, when the mass ratio of KOH/CGFS increases further, the over-dosed potassium vapor can cause the collapse and reorganization of a large number of skeleton carbon [24], leading to a decrease in graphitization degree and an increase in the $I_{\text{D}}/I_{\text{G}}$ value [36]. Among them, the recombination of carbon in the CGFS-AC (1:4) sample is more obvious with fewer internal structural defects, showing better structural properties. The illustration in inset of Fig. 4 is the three-dimensional Raman

**Fig. 4** Raman spectra of CGFS and CGFS-AC, inset is the three-dimensional Raman mapping of CGFS-AC (CGFS/KOH = 1:4)

mapping inset of CGFS-AC (1:4), a good uniformity of material can be found.

3.3 Electrochemical characterizations

3.3.1 Electrochemical behaviors of CGFS-AC electrode in a three-electrode system

To obtain the electrochemical behavior of CGFS-AC electrodes prepared under different CGFS/KOH conditions, 6 M KOH was applied as the electrolyte in a three-electrode system. CV measurement at 25 mV/s and GCD test at 1 A/g of CGFS-AC electrode materials are presented in Fig. 5a and b. The CV curves show an approximate rectangular shape and GCD curves present a nearly triangle, indicating that CGFS-AC is ideal electrode material for electric double-layer capacitors. The inset in Fig. 5a shows the area surrounded by CV curve with various CGFS/KOH ratios. CGFS-AC (1:4) sample possesses the largest surrounding area and longest discharge time than the other four electrode materials, indicating that the CGFS-AC (1:4) electrode material shows the best electrochemical behaviors. As shown in Fig. 5c, the specific capacitance of CGFS-AC are 284.6 (1:2), 306.4 (1:3), 384.4 (1:4), 287.5 (1:5), and 286.7 F/g (1:6) at 1 A/g, which confirm that CGFS-AC (1:4) sample has best capacitive property. The results of specific capacitance at different current densities for CGFS-AC electrode prepared under different CGFS/KOH conditions are shown in Table 5.

EIS test is an important technique for studying the charge transfer and electrolyte diffusion in the electrode/electrolyte interface. As shown in Fig. 5d, the Nyquist plot of all CGFS-AC electrode materials are composed of a semicircle in the high-frequency region, a straight line with a slope of 45° in the middle-frequency region, and a linear region almost 90° at low frequencies. The equivalent circuit in the inset is simulated by Z_{view} software [37]. Here, the circuit model is composed of the equivalent series resistance (R_s), charge transfer resistance (R_{ct}), double-layer capacitance (C), and Warburg diffusion resistance (Z_w) [38]. As can be seen, the CGFS-AC (1:4) has a lower charge transfer resistance (R_{ct}) value (2.04 Ω) than CGFS-AC (1:2) (6.99 Ω), CGFS-AC (1:3) (3.01 Ω), CGFS-AC (1:5) (3.67 Ω), and CGFS-AC (1:6) (5.87 Ω), which shows that the CGFS-AC (1:4) has facile charge transfer at the electrode/electrolyte interface due to its hierarchical porous structure and

a large number of mesopores (largest specific surface area of 1151.8 m²/g, pore volume of 0.923 cm³/g and mesoporosity of 78.5%). According to the simulation of the equivalent circuit diagram, the R_s for CGFS-AC (1:4) is found to be 0.69 Ω , which is slightly lower than that of the CGFS-AC (1:2) (3.23 Ω), CGFS-AC (1:3) (0.71 Ω), CGFS-AC (1:5) (0.74 Ω), and CGFS-AC (1:6) (2.36 Ω). Moreover, the CGFS-AC (1:4) has a lower Z_w value (0.28 Ω) than CGFS-AC (1:2) (1.87 Ω), CGFS-AC (1:3) (0.29 Ω), CGFS-AC (1:5) (0.35 Ω), and CGFS-AC (1:6) (0.41 Ω), indicating that the appropriate micropores and abundant mesopores are more conducive to electrolyte ion diffuses, thereby helping to expand the capacitance. The slope of CGFS-AC (1:4) electrode material in the low frequency region is significantly higher than that of other CGFS-AC, which is the closest to 90°, indicating that the electrolyte ion diffusion/migration process to the electrode surface is the fastest. It can be attributed that in the hierarchical pore structure of CGFS-AC, micropores can provide a large specific surface area for ion storage, and mesopores and macropores provide effective ion transport channels. This result is consistent with the analysis result of pore structure. Obviously, the CGFS-AC (1:4) is one of the more promising candidates to be used as an electrode material for supercapacitors as evidenced from the CV, GCD, and EIS measurements.

The electrochemical behaviors of optimal CGFS-AC (1:4) electrode in a three-electrode system are further assessed by CV tests at different scan rates, GCD measurements at various current densities, EIS test, and cycling stability tests for 10,000 cycles. As revealed in Fig. 6a, CV curves of CGFS-AC (1:4) display a nearly rectangular shape at low scan rates. As the scan rate increases, the curve still presents an approximate rectangle, indicating that this material has the efficient double-layer charge storage. In addition, the linear relationship between the peak current and the scan rate is shown in the inset of Fig. 6a, which confirms that the charge storage mechanism is mainly based on the surface charge adsorption–desorption process [39]. The GCD curve of Fig. 6b is approximately triangular, which indicates that it is an ideal electric double-layer capacitor material. Figure 6c shows the specific capacitance of CGFS-AC (1:4) are 384.4, 228.4, 188.5, 171.2, 154.4, 148.5, and 130.6 F/g at current densities from 1 to 50 A/g, respectively. Figure 6d displays the Nyquist plots of CGFS-AC (1:4). The equivalent series resistance of R_s is 0.69 Ω , the charge transfer resistance

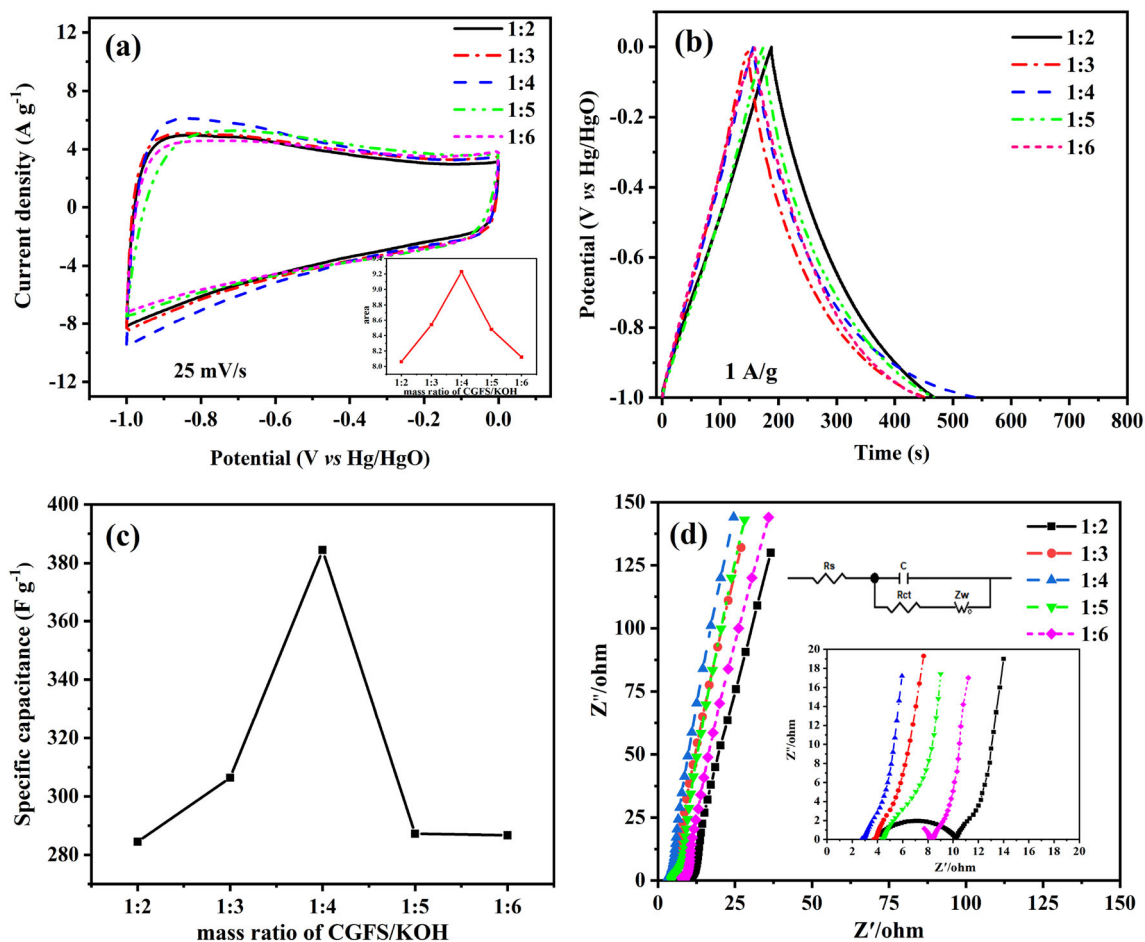


Fig. 5 Electrochemical characterization of CGFS-AC in three-electrode system, **a** CV curves at 25 mV/s, **b** GCD curves at a current density of 1 A/g, **c** The specific capacitance at different

CGFS/KOH ratios at 1 A/g, **d** Nyquist plots of CGFS-AC electrodes, the insets show their equivalent circuit and the magnified impedance in the high-frequency region of the samples

Table 5 Specific capacitances of CGFS-AC at different current densities

Current density (A/g)	Specific capacitance (F/g)				
	CGFS/KOH = 1/2	CGFS/KOH = 1/3	CGFS/KOH = 1/4	CGFS/KOH = 1/5	CGFS/KOH = 1/6
1	284.6	306.4	384.4	287.5	286.7
2	220.8	206.4	228.4	228.7	202.8
5	185.5	171.7	188.5	194.5	169.1
10	152.9	153.2	171.2	172.9	144.4
20	113.8	136.5	154.4	147.8	116.2

of R_{ct} is 2.04 Ω , and the Warburg diffusion resistance of Z_w is only 0.28 Ω , which show that lower resistance is conducive to the rapid transfer of charge.

Figure 6e shows the specific capacitance of CGFS-AC (1:4) material at 5 A/g as a function of cycles number. It is worth noting that the specific

capacitance basically remains unchanged at 188.5 F/g after 6800 cycles, which is 100% of the initial specific capacitance. The last 10 GCD cycles are also drawn in the inset of Fig. 6e, showing that this material has good reversibility during the GCD process. In addition, the coulombic efficiency is changed

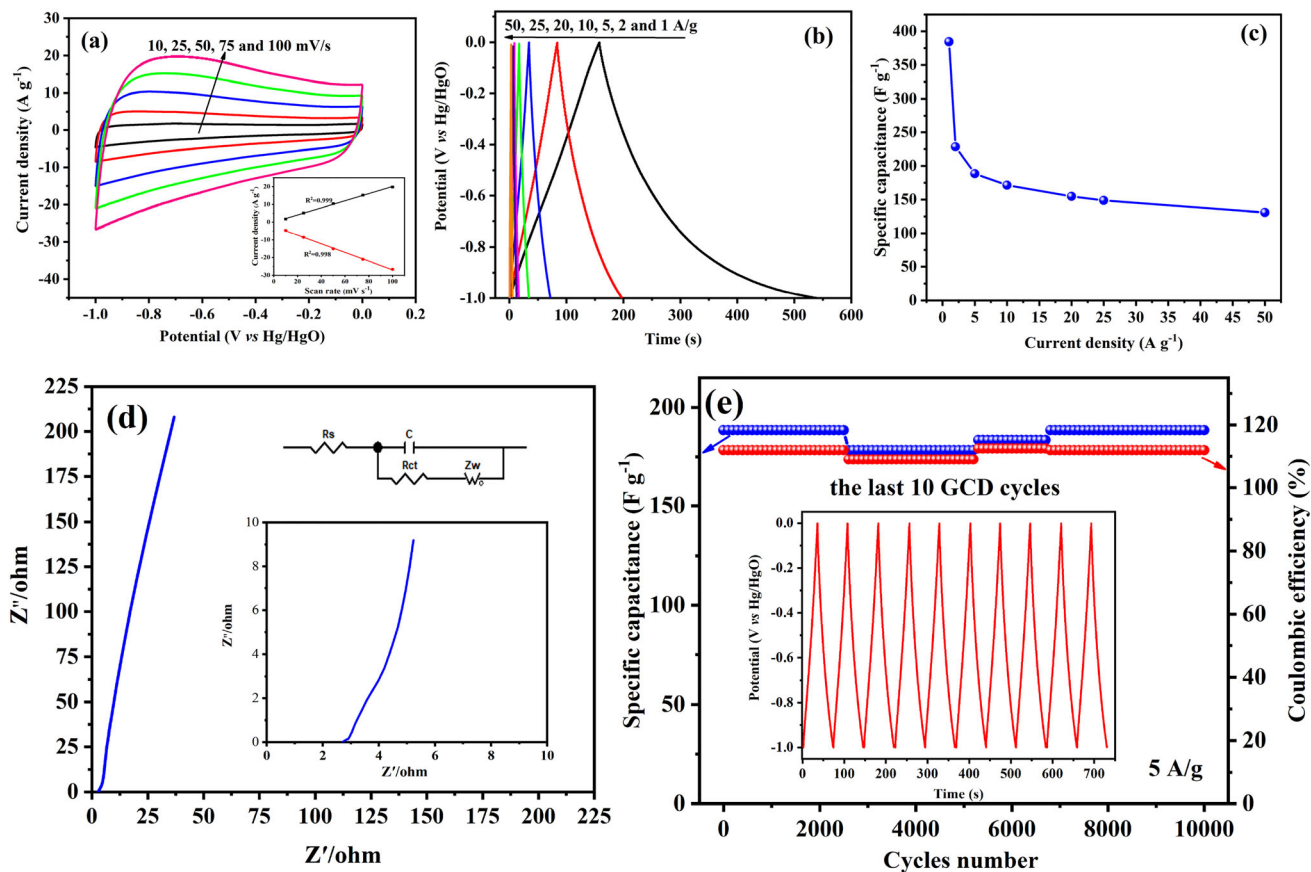


Fig. 6 Electrochemical characterization of CGFS-AC (1:4) in three-electrode system. **a** CV curves at 10–100 mV/s, inset: linear response of the peak current intensity *vs* the scan rates, **b** GCD curves at different current densities of 1 and 50 A/g, **c** The specific

capacitance at different current densities, **d** The Nyquist plot and **e** cycling stability and coulombic efficiency at 5 A/g, inset: the last 10 GCD cycles

slightly in the process of 10,000 cycling and reached to 112% at the end of test, which proves that K^+ ions have highly reversible adsorption/desorption on the surface of CGFS-AC pores and have an outstanding cycle-life. In summary, CGFS-AC (1:4) electrode material has high specific capacitance and excellent cycle stability, indicating that this material is suitable for assembling supercapacitors.

3.3.2 Electrochemical behaviors of CGFS-AC//CGFS-AC symmetric supercapacitor in a two-electrode system

In order to explore the practical application of CGFS-AC (1:4) material, a symmetric supercapacitor was assembled. Steady voltammograms of CGFS-AC//CGFS-AC symmetric supercapacitor toward positive potentials is shown in Fig. 7a. It can be seen that these CV curves show a rectangular shape related to the formation of the electric double layer. As the upper

potential limit increases, the peak current of the positive potential also increases. When the operating voltage window is increased to 1.6 V, no oxidation of the carbon material is observed in the CV curves. When the voltage is increased to 1.8 V, the high voltage position curve has a sudden increase, indicating that the test supercapacitor has been polarized. If the highest potential is maintained for a long time, the carbon material may be degraded [40]. Therefore, the optimal voltage window range of CGFS-AC//CGFS-AC symmetric supercapacitor is set to 1.6 V. In Fig. 7b, the CV shape hardly changes with the increase of the scan rate, which means that the CGFS-AC//CGFS-AC symmetric supercapacitor has excellent capacitance performance and reversibility. GCD curves of the CGFS-AC//CGFS-AC symmetric supercapacitor are shown in Fig. 7c. During the charge process of CGFS-AC//CGFS-AC symmetric supercapacitor, OH^- ions accumulate on the interface of CGFS-AC

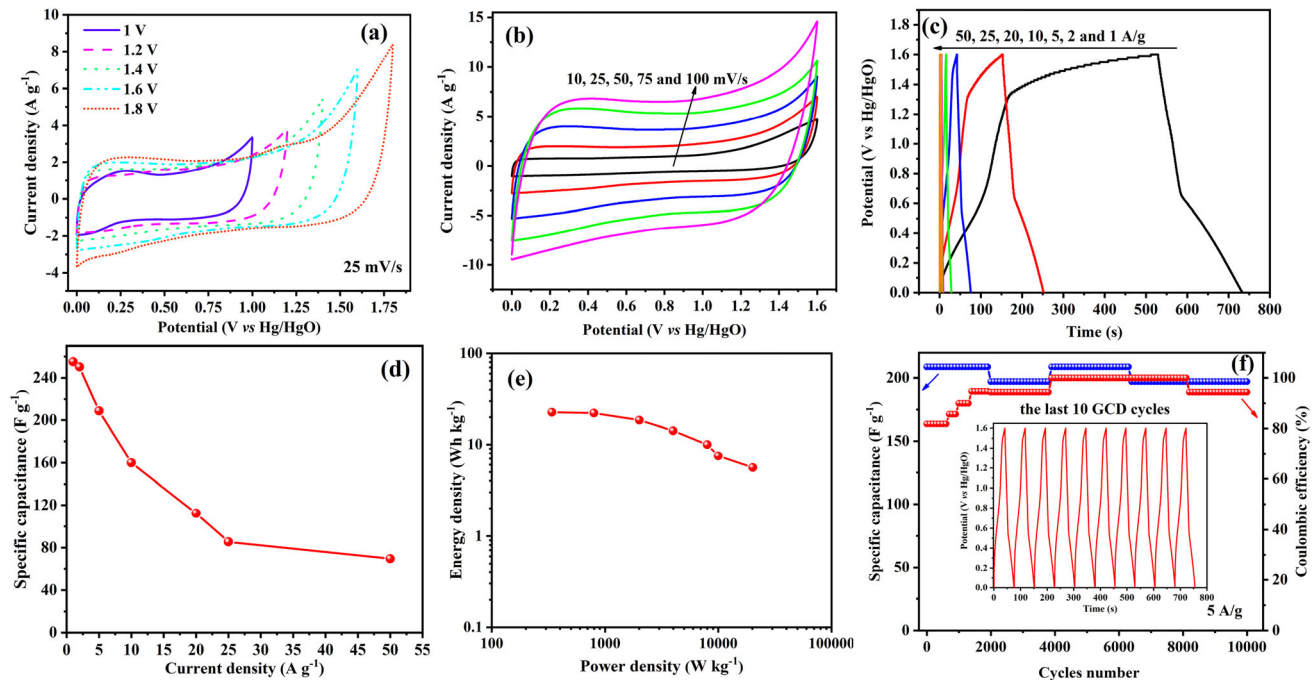


Fig. 7 Electrochemical characterization of CGFS-AC//CGFS-AC symmetric supercapacitor in a two-electrode system. **a** Steady voltammograms of positive potentials, **b** CV curves, **c** GCD

curves, **d** rate capability, **e** Ragone plot and **f** cycling stability and coulombic efficiency at 5 A/g, inset: the last 10 GCD cycles

cathode/electrolyte, while K^+ ions are inserted into the anode of CGFS-AC. The corresponding specific capacitance is calculated from the discharge time at each current density and plotted in Fig. 7d. Herein, the specific capacitance of CGFS-AC//CGFS-AC symmetric supercapacitor are 255.2, 250.2, 208.7, 160.2, 112.5, 84.4, and 62.5 F/g at 1, 2, 5, 10, 20, 25, and 50 A/g, respectively, which are superior to the charge storage capacity of commercial activated carbon (YP-50F, 100–160 F/g at 0.5 A/g) [41, 42]. Furthermore, it can be observed from Fig. 7e that the Ragone plot of CGFS-AC//CGFS-AC symmetric supercapacitor shows a high energy density of 22.7 Wh/kg at a power density of 399.8 W/kg. The long-term cycling stability of a CGFS-AC//CGFS-AC symmetric supercapacitor is shown in Fig. 7f. Its capacitance remains 197.1 F/g (94.4% of the initial value) after 6400 cycles, and 197.1 F/g after 10,000 cycles at 5 A/g, showing excellent cycling stability. In addition, the coulombic efficiency remains over 80% during 10,000 cycles, and remains at 94% after 8200 cycles, indicating that the symmetric supercapacitor has a higher discharge efficiency. Based on the above analysis, CGFS-AC//CGFS-AC symmetric supercapacitor has high storage capacity, high energy density and excellent cycling stability, which is beneficial to practical applications.

4 Conclusion

In summary, we have prepared a CGFS-based activated carbon material, which exhibits superior electrochemical and capacitive performance, benefiting from its multi-stage hierarchical structure. The hierarchical structure of mesopores/micropores facilitates the rapid transmission of ions between the internal surface and the external electrolyte solution. The CGFS-AC (1:4) has the largest specific surface area ($1151.8 \text{ m}^2/\text{g}$), largest pore volume ($0.923 \text{ cm}^3/\text{g}$), and highest mesoporosity (78.5%). Due to CGFS-AC (1:4) owning larger mesopores volume, it has higher specific capacitance (384.4 F/g at 1 A/g), excellent cycling stability (the specific capacity remains 94.4% after 10,000 cycles), and coulombic efficiency (remains at 112% after 10,000 cycles). The assembled symmetric supercapacitor has high specific capacitance (255.2 F/g at 1 A/g), energy density (22.2 Wh/kg), and cycle stability (94.4% of the initial capacitance). The CGFS-AC material can be served as promising electrode material for supercapacitors. In addition, the recycling and high value-added utilization of solid waste in gasification process are realized.

Acknowledgements

Authors thank for financial support by Shaanxi Province Technological Innovation Guidance Special (2021QFY04-01) and technical support by Analytical Instrumentation Center of XUST.

Author contributions

NY contributed to conceptualization, investigation, methodology, data curation, and writing of the original draft. SX contributed to supervision, funding acquisition, and reviewing and editing of the manuscript. XW contributed to visualization and formal analysis of the manuscript. MG contributed to methodology and resources. JC contributed to conceptualization of the manuscript. RZ contributed to project administration of the manuscript. BW contributed to supervision of the manuscript. ZL contributed to funding acquisition of the manuscript. JX contributed to validation of the manuscript. All authors have read and agreed to the published version of the manuscript.

Data availability

My manuscript has no associated data. All data generated or analyzed during this study are included in the manuscript.

Declarations

Conflict of interest As a corresponding author, I state that we don't have any conflict of interest to our research paper.

References

1. X. Liu, Z.J. Zhou, F.C. Wang, The effect of industry slag on coal water slurry and gasification. *Energy Sour., A: Recover., Utilization, Environ. Eff.* **36**(17), 1871–1876 (2014)
2. X. Zhao, C. Zeng, Y. Mao et al., The surface characteristics and reactivity of residual carbon in coal gasification slag. *Energy Fuels* **24**(1), 91–94 (2010)
3. T. Wu, M. Gong, E. Lestre et al., Characterisation of residual carbon from entrained-bed coal water slurry gasifiers. *Fuel* **86**(7–8), 972–982 (2007)
4. Y. Gu, X. Qiao, A carbon silica composite prepared from water slurry coal gasification slag. *Microporous Mesoporous Mater.* **276**(2), 303–307 (2019)
5. C. Pan, Q. Liang, X. Guo et al., Characteristics of different sized slag particles from entrained-flow coal gasification. *Energy Fuels* **30**(2), 1487–1495 (2016)
6. J. Ratafia-Brown, Major environmental aspects of gasification-based power generation technologies. Office of Scientific & Technical Information Technical Reports, 1–24 (2002)
7. S. Zhao, Preparation and environmental toxicity of non-sintered ceramsite using coal gasification coarse slag. *Arch. Environ. Prot.* **45**(2), 84–90 (2019)
8. A. Acosta, I. Iglesias, M. Aineto et al., Utilisation of IGCC slag and clay steriles in soft mud bricks (by pressing) for use in building bricks manufacturing. *Waste Manag. (New York, NY)* **22**(8), 887–891 (2002)
9. S. Wu, S. Huang, L. Ji et al., Structure characteristics and gasification activity of residual carbon from entrained-flow coal gasification slag. *Fuel* **122**(4), 67–75 (2014)
10. J. Zhang, J. Zuo, W. Ai et al., Preparation of a new high-efficiency resin deodorant from coal gasification fine slag and its application in the removal of volatile organic compounds in polypropylene composites. *J. Hazard. Mater.* **384**(2), 121347–121359 (2019)
11. Y. Gu, X. Qiao, A carbon silica composite prepared from water slurry coal gasification slag. *Microporous Mesoporous Mater.* **276**(18), 303–307 (2018)
12. H. Yin, Y. Tang, Preparation of Ca- α -sialon-SiC multiphase ceramics from gasification slag. *Mater. Sci. Forum* **695**(28), 328–331 (2011)
13. Y. Tang, H. Yin et al., Phase and morphological transformation stages during carbothermal reduction nitridation process: from coal gasification slag wastes to Ca- α -SiAlON powders. *Adv. Powder Technol.* **27**(5), 2232–2237 (2016)
14. F. Han, Y. Gao, Q. Huo et al., Characteristics of vanadium-based coal gasification slag and the NH₃-selective catalytic reduction of NO. *Catalysts* **8**(8), 327–343 (2018)
15. S. Wu, S. Huang, Y. Wu et al., Characteristics and catalytic actions of inorganic constituents from entrained-flow coal gasification slag. *J. Energy Inst.* **88**(1), 93–103 (2015)
16. F. Teoh, A. Veksha, V. Chia et al., Nickel-based catalysts for steam reforming of naphthalene utilizing gasification slag from municipal solid waste as a support. *Fuel* **254**(15), 115561–115561 (2019)
17. W. Ai, S. Liu, J. Zhang et al., Mechanical and nonisothermal crystallization properties of coal gasification fine slag glass bead-filled polypropylene composites. *J. Appl. Polym. Sci.* **136**(7), 47803–47814 (2019)
18. D. Dong, Y. Zhang, Y. Xiao et al., High performance aqueous supercapacitor based on nitrogen-doped coal-based activated

- carbon electrode materials. *J. Colloid Interface Sci.* **580**(15), 77–87 (2020)
19. X.M. Yue, Z.Y. An, M. Ye et al., Preparation of porous activated carbons for high performance supercapacitors from taixi anthracite by multi-stage activation. *Molecules* **24**(19), 3588–3603 (2019)
 20. S. Xiong, Y. He, X. Wang et al., Ultralow ash semicoal powder obtained by two-step acid treatment and its supercapacitive properties. *Energy Fuels* **34**(6), 7591–7599 (2020)
 21. F. Wei, H. Zhang, X. He et al., Synthesis of porous carbons from coal tar pitch for high-performance supercapacitors. *New Carbon Mater.* **34**(2), 132–139 (2019)
 22. V. Choudhry, S.R. Hadley, Utilization of coal gasification slag. *Clean Energy Waste and Coal* **515**(20), 253–263 (1992)
 23. R. Andrews, A. Rubel, J. Groppo et al., Advanced gasification by-product utilization. Office of Scientific & Technical Information Technical Reports, 1–24 (2021)
 24. S. Xu, Z. Zhou, X. Gao et al., The gasification reactivity of unburned carbon present in gasification slag from entrained-flow gasifier. *Fuel Process. Technol.* **90**(9), 1062–1070 (2009)
 25. X. Guo, Z. Dai, X. Gong et al., Performance of an entrained-flow gasification technology of pulverized coal in pilot-scale plant. *Fuel Process. Technol.* **88**(5), 451–459 (2007)
 26. Y. Xu, X. Chai, Characterization of coal gasification slag-based activated carbon and its potential application in lead removal. *Environ. Technol.* **39**(3), 382–391 (2018)
 27. Z. Miao, Z. Guo, G. Qiu et al., Synthesis of activated carbon from high-ash coal gasification fine slag and their application to CO₂ capture. *J. CO₂ Util.* **50**(13), 101585–101594 (2021)
 28. H. Zhao, L. Wang, D. Jia et al., Coal based activated carbon nanofibers prepared by electrospinning. *J. Mater. Chem. A* **2**(24), 9338–9344 (2014)
 29. S. Dong, X. Ji, M. Yu et al., Direct synthesis of interconnected porous carbon nanosheet/nickel foam composite for high-performance supercapacitors by microwave-assisted heating. *J. Porous Mater.* **25**(3), 923–933 (2017)
 30. Y. Liu, G. Li, Y. Guo et al., Flexible and binder-free hierarchical porous carbon film for supercapacitor electrodes derived from MOFs/CNT [J]. *ACS Appl. Mater. Interfaces.* **9**(16), 14043–14050 (2017)
 31. H. Wu, J. Yang, H. Chen et al., Revealing the nanodomain structure of silicon oxycarbide via preferential etching and pore analysis. *Funct. Mater. Lett.* **9**(3), 1650043.1–1650043.5 (2016)
 32. H. Chen, Y. Ai, L. Fan et al., Carbon-coated hierarchical Ni–Mn layered double hydroxide nanoarrays on Ni foam for flexible high-capacitance supercapacitors. *Electrochim. Acta* **213**(16), 55–65 (2016)
 33. C. Fan, H. Ma, L. Hua, Spectroscopic analysis analysis of the crystallization mechanism of synthesized zeolite with XRD and FTIR approaches. *Guang pu xue yu guang pu fen xi Guang pu* **32**(4), 1118–1122 (2012)
 34. R. Farzana, R. Rajarao, B.R. Bhat et al., Performance of an activated carbon supercapacitor electrode synthesised from waste compact discs (CDs). *J. Ind. Eng. Chem.* **65**(18), 387–396 (2018)
 35. D. Zhao, H. Liu, D. Zhu et al., Effect of O-containing functional groups produced by preoxidation on Zhundong coal gasification. *Fuel Process. Technol.* **206**(7), 106480–106491 (2020)
 36. Z. Miao, G. Qiu, X. Zhao et al., Influence of pre-oxidization on the characterizations of coal gasification fine slag-derived activated carbons for CO₂ capture. *J. CO₂ Util.* **54**(10), 101754–101763 (2021)
 37. S. Xiong, F. Yang, H. Jiang et al., Covalently bonded polyaniline/fullerene hybrids with coral-like morphology for high-performance supercapacitor. *Electrochim. Acta* **85**(8), 235–242 (2012)
 38. Y. Zhou, Z. Mao, W. Wang et al., In-situ fabrication of graphene oxide hybrid Ni-based metal-organic framework (Ni-MOFs@GO) with ultrahigh capacitance as electrochemical pseudocapacitor materials. *ACS Appl. Mater. Interfaces.* **8**(42), 28904–28916 (2016)
 39. W. Cao, F. Yang, Supercapacitors from high fructose corn syrup-derived activated carbons. *Mater. Today Energy* **9**(6), 406–415 (2018)
 40. I. Pi Eiro-Prado, D. Salinas-Torres, R. Ruiz-Rosas et al., Design of activated carbon/activated carbon asymmetric capacitors. *Front. Mater.* **3**(16), 16–28 (2016)
 41. R.K. Gupta et al., Biochar activated by oxygen plasma for supercapacitors-ScienceDirect. *J. Power Sourc.* **274**(15), 1300–1305 (2015)
 42. D. Zhang, M. Han, Y. Li et al., Ultra-facile fabrication of phosphorus doped egg-like hierarchic porous carbon with superior supercapacitance performance by microwave irradiation combining with self-activation strategy-ScienceDirect. *J. Power Sourc.* **372**(6), 260–269 (2017)

Publisher's Note Springer Nature remains neutral with regard to jurisdictional claims in published maps and institutional affiliations.